Supporting Information

Nelson et al. 10.1073/pnas.1009194108

SI Materials and Methods

Chronological Tuning. Uncertainty in radiocarbon chronology becomes problematic when attempting to correlate high-resolution paleoenvironmental records on submillennial time scales. Minor tuning procedures were conducted in the Analyseries software platform to correlate the portions of the record where age control was more vague (e.g., in the vicinity of the radiocarbon dated material). Tuning was justified on the basis of strong agreement between the following data: the Castor Lake $\delta^{18}O$ record and the regional 20th century Palmer Drought Severity Index (PDSI) values (Fig. 1), the sediment grayscale data and the $\delta^{18}O$ data from all sections of the record (Fig. 2 and Figs. S1 and S2), and also the grayscale data and the reconstructed PDSI values near the well-dated Mount Saint Helens W tephra event (Fig. S3). All age adjustments were well within the 2σ error range of the radiocarbon measurements. Additional dating uncertainties, as well as noise (i.e., variability resulting from short-term, interannual climate variations as well as analytical errors and data without a climatic origin) present in both records, were addressed by using 20-yr low-pass filtered time series data. Tree-ring based PDSI reconstruction data were obtained both as raw data and as 20-yr low-pass filtered timeseries from the National Oceanic and Atmospheric Administration (NOAA) World Data Center (WDC) for Paleoclimatology. Grayscale data were filtered using a 3rd order Butterworth low-pass.

To reduce correlation bias after tuning, the artificial skill (i.e., random correlation) between the records was calculated by averaging the correlation coefficients obtained by comparing the PDSI time series with several portions of the grayscale record that were older than the earliest date represented in the PDSI data, and thus must have no physical correlation. The average artificial skill ($r = -0.03$) was then subtracted from the raw correlation coefficient obtained between the temporally matched portions of the records ($r = -0.70$) to obtain an adjusted r-value of −0.67. Degrees of freedom (DOF) in the correlation were determined by calculating the nominal decorrelation time-scale (i.e., the number of lags required for the autocorrelation function of each series to decay to zero). As a conservative estimate, the larger decorrelation time-scale obtained from the PDSI series was used to calculate the number of DOF for the correlation between the grayscale record and PDSI ($n - 2/$ decorrelation time-scale $= 53$). The adjusted r-value and adjusted DOF were then used to calculate $p < 0.0001$, or significance beyond the 99.99% level.

Chronology. Samples of charcoal or identifiable terrestrial macrofossils, including seeds from the *Cyperaceae* sedge family, were used for radiocarbon measurements. Analyses were conducted at the W.M. Keck Carbon Cycle Accelerator Mass Spectrometry Laboratory at the University of California, Irvine (UCI), and the Center for Accelerator Mass Spectrometry (CAMS) at Lawrence Livermore National Laboratory. Samples sent to the UCI lab were pretreated at the University of Pittsburgh following standard acid-base-acid procedures (1). All radiocarbon ages were calibrated using the CALIB online software program version 4.4.2 (2).

Several tephra layers were present in the sediment sequence, although many were very thin and not readily identifiable with the unaided eye. Samples of two tephras of significant thickness were sent to Washington State University for identification by electron microprobe. The first of these tephras was identified as the Mount Saint Helens (MSH) W ash with an age of 1480 A.D. (470 B.P.) as determined by dendrochronology (3). The second tephra is from the Mazama climactic eruption in Oregon ca. $6{,}730 \pm 40$ ^{14}C yr B.P. (7,585 cal yr B.P.) (4).

^{210}Pb and ^{137}Cs activity measurements were made at the Freshwater Institute at the University of Manitoba in Winnipeg, Canada. The age model generated through the application of the constant rate of supply (CRS) model to the measured ^{210}Pb activities did not include the ^{137}Cs peak at 1964, even within a 2σ error range. Although ^{137}Cs can be mobile in the sediment column, it is unlikely that this occurred in Castor Lake, given the laminated nature of the sediments and the relatively low organic matter content (10–20%) in the upper sequence of the core. A more likely explanation for the discrepancy between the ^{137}Cs and the ^{210}Pb dates is that variation in supported ^{210}Pb has introduced inaccuracies to the CRS age model. Because no proxy for supported ^{210}Pb was measured, such as ^{226}Ra, the average asymptotic value of ^{210}Pb activity at depth was used as an estimate for supported ^{210}Pb throughout the entire sequence. Whereas this commonly applied approach is often successful, it may account for the age discrepancies in this case. Due to the ambiguous nature of the ^{210}Pb profile, the ^{137}Cs profile was used in favor of the ^{210}Pb as the basis for the final age model in the upper section of the Castor Lake sediment record.

The ^{137}Cs profile matched the typical pattern of increase through the 1950s to 1964 A.D., when atmospheric nuclear testing was banned and ^{137}Cs levels began to decline. A date of 1964 A.D. was assigned to the depth of the ^{137}Cs activity peak, and a date of 1959 A.D. was assigned to the beginning of the ^{137}Cs increase based on the shape of established atmospheric activity curves. A linear relationship was then assumed between sediment age and depth from the top of the sediment (2003 A.D.), through the two cesium-inferred dates, down to the point corresponding to 1954 A.D. The assumed linearity over this interval is based on trends in sediment density, which change at the 1954 A.D. level, indicating a probable end to the linear relationship that exists between age and depth in the upper ∼50 yr of the sediment.

The final set of age control data (Table S1) were then used to construct an age-depth model (Fig. S6) on the basis of linear regression between control points. Two radiocarbon ages in close proximity to the well-dated tephra layers described above were excluded from the model. In both cases there were minor disagreements between the radiocarbon and tephra ages.

Sediment Color and Grayscale. Digital images of clean (i.e., freshly surfaced split cores) were collected with a Pixera© Pro 150 ES camera equipped with a Optem International© macro video zoom lens under controlled light conditions. Down-core transects of red-green-blue (RGB) values were then generated with single pixel size resolution using a macro program written for the National Institutes of Health image software platform. Each transect was averaged over 50 pixels in width, and care was taken to collect data over representative sections to avoid collecting color data that did not reflect sediment composition (e.g., cracks, gaps, etc.). Transect data were then spliced together in NIH software and exported. Data were down-sampled to an even 1-yr time step to reduce the dataset to a workable size. RGB data were averaged to create a single digital number (DN) value (grayscale) that was normalized to the mean to facilitate signal processing and comparison with other datasets (Fig. S7).

The time series exhibited several ambiguous millennial-scale trends that were likely the result of diagenetic processes and laboratory handling artifacts unique to grayscale. The data were

therefore detrended using singular spectrum analysis (SSA) ($M = 150$) (5, 6) (Fig. S7). This procedure emphasized centennial and shorter-scale variability, and probably resulted in the loss of some climate-driven millennial-scale features in the data. However, this was an unavoidable consequence of the need to remove the nonclimatic components of the record.

Stable Isotopes. Bulk lake sediment samples were treated overnight with 7% H_2O_2 to disaggregate and remove oxidized organic matter. Samples were wet-sieved to collect the <63 μm carbonate fraction for isotope analysis. The sediment sieve water containing the <63 μm fractions was transferred to containers and allowed to settle from solution. The sieve water was then centrifuged to concentrate the <63 μm fraction, which was then bleached and rinsed with deionized water to further purify the carbonate. After bleaching, the samples were freeze-dried and homogenized with a mortar and pestle.

The majority of isotopic analyses of treated carbonate samples were conducted at the University of Pittsburgh on a GV Instruments IsoPrime stable isotope ratio mass spectrometer equipped with a dual inlet, MultiPrep inlet module, and Gilson autosampler. Samples were measured against National Institute of Standards and Technology (NIST) carbonate standard material NBS-18 and NBS-19 and reported relative to the Vienna Pee Dee belemnite isotope scale in standard per mil notation. Internal precision was better than 0.05‰ for carbon and 0.1‰ for oxygen. Replicate sample analyses were performed on approximately 10% of samples, with average differences of 0.06‰ for carbon and 0.12‰ for oxygen. Laboratory backlog required that some samples be sent to the University of Florida, as well as the University of Saskatchewan. At the University of Florida, samples were measured on a Finnegan-MAT 252 mass spectrometer and Kiel III automated preparation system. Analytical precision, measured against NBS-19 reference materials, was better than 0.02‰ for carbon and 0.06‰ for oxygen. Samples measured at the University of Saskatchewan were analyzed using a Finnegan-Mat 253 mass spectrometer and Kiel device, and measured against an internal standard, USC-1, which was stringently calibrated to NBS-19. Analytical precision was 0.05‰ for carbon and 0.11‰ for oxygen. Replicate analyses were performed at the University of Pittsburgh on approximately 10% of the sample total analyzed at Saskatchewan. Interlaboratory error was 0.07‰ for carbon and 0.08‰ for oxygen. No similar comparison was performed for the samples analyzed at the University of Florida. However, disparate samples from stratigraphically overlapping cores were sampled and analyzed in each laboratory.

The composite $\delta^{18}O$ and $\delta^{13}C$ time series data were resampled at an even 5-yr time step (i.e., the average time step based on the measured sampling interval) using linear interpolation to prepare the data for detrending in the exact manner as the grayscale data. This was done to maintain consistency in the treatment of each time series. In the stable isotope data, the millennial-scale trends removed by this process were minor, with even the raw data showing little change in mean values over the period of record (Fig. S8).

1. Abbott MB, Stafford TW (1996) Radiocarbon geochemistry of ancient and modern Arctic lakes, Baffin Island. *Quaternary Res* 45:300–311.
2. Stuiver M, Reimer PJ, Braziunas TF (1998) High-precision radiocarbon age calibration for terrestrial and marine samples. *Radiocarbon* 40:1127–1151.
3. Mullineaux DR (1986) Summary of pre-1980 tephra-call deposits erupted from Mount St. Helens, Washington State, USA. *B Volcanol* 4817:17–26.
4. Hallett DJ, Hills LV, Clague JJ (1997) New accelerator mass spectrometry radiocarbon ages for the Mazama tephra layer from Kootenay National Park, British Columbia, Canada. *Can J Earth Sci* 34:1202–1209.
5. Ghil M, et al. (2002) Advanced spectral methods for climatic time series. *Rev Geophys* 40(1):3.1–3.41, 10.1029/2000RG000092.
6. Dettinger MD, Ghil M, Strong CM, Weibel W, Yiou P (1995) Software expedites singular-spectrum analysis of noisy time series. *Eos Trans American Geophysical Union* 76:12, 14, 21.

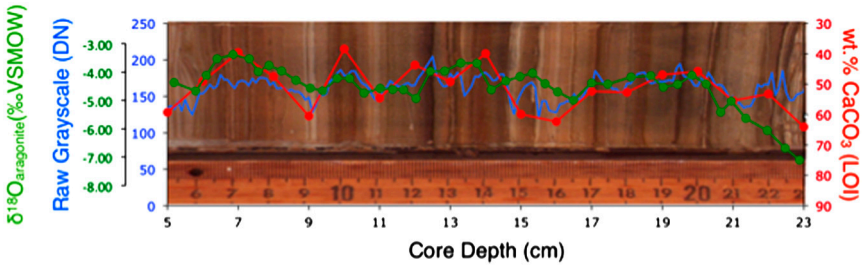

Fig. S1. Sample core image showing relationships between grayscale (blue), $\delta^{18}O$ (green), and loss-on-ignition wt.% $CaCO_3$ (red) as a function of depth. Note the inverted scale of the loss-on-ignition wt.% $CaCO_3$ axis. Higher grayscale values correspond to higher $\delta^{18}O$ values and lower wt.% $CaCO_3$ as described in the text. The sampling resolution of the grayscale data (1 pixel) captures sediment changes recorded by $\delta^{18}O$ and wt.% $CaCO_3$, though at a much finer scale than the latter two datasets, which were sampled at 2–3 mm scale, and 1 cm scale, respectively.

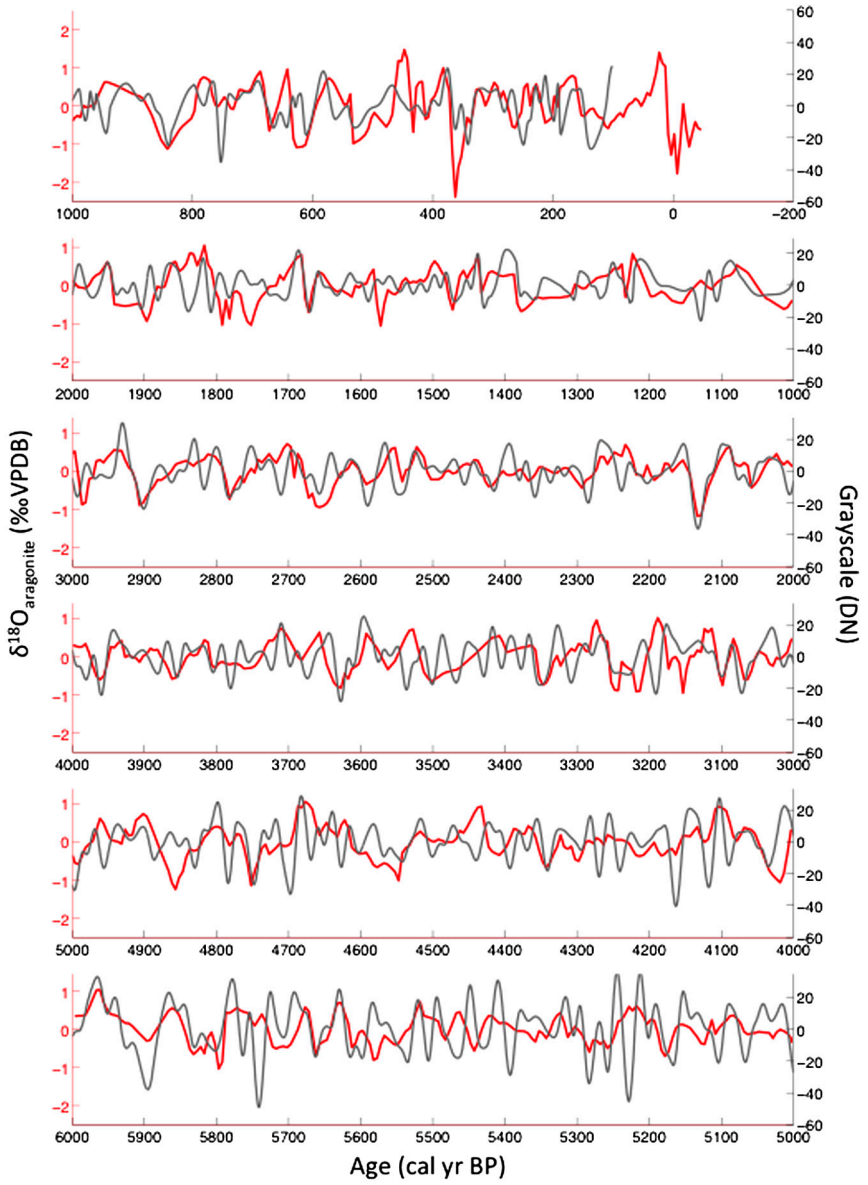

Fig. S2. Comparison of the Castor Lake grayscale (gray) and $\delta^{18}O$ (red) data. The data shown here are identical to those presented in Fig. 2 in the main text, but here the plot is expanded to six 1000-yr increments so that more detailed comparison of the two records is possible.

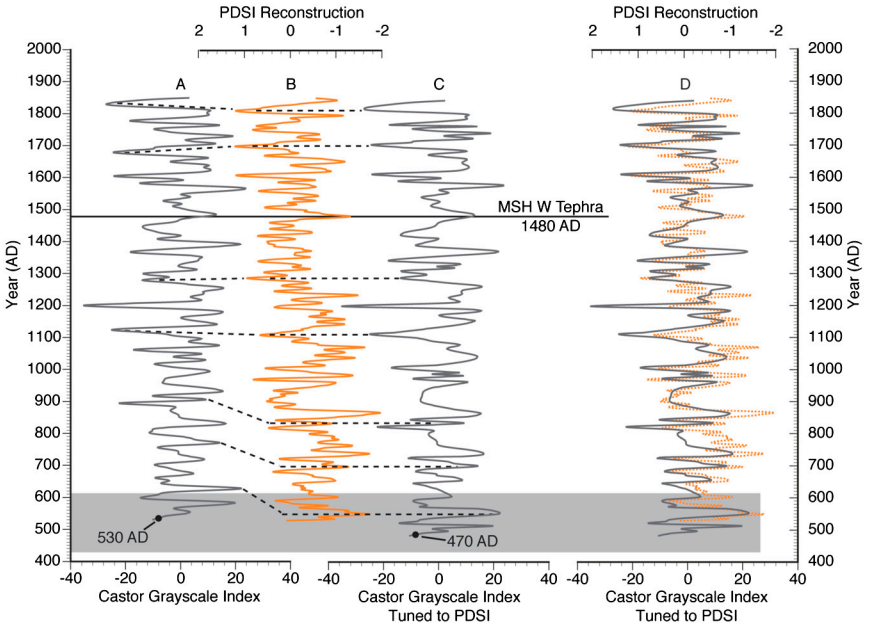

Fig. S3. Castor Lake grayscale tuning to PDSI. All data presented after 20-yr low-pass filter. *X*-axes are scaled to show increasing aridity to the right. The horizontal bar at 1480 A.D. represents the Mount Saint Helens W tephra unit. (*A*) Untuned grayscale time series. The radiocarbon age is shown as a black circle, with the gray bar representing 2σ error. (*B*) PDSI reconstruction from NOAA WDC (1). (*C*) Tuned Castor Lake grayscale record. New depth of the radiocarbon age is shown as a black circle. Representative tie-points are shown as dashed lines between panels A, B, and C. (*D*) Tuned grayscale record (solid gray line) overlay on the PDSI reconstruction (dashed orange line) (DOF = 53, adjusted $r = -0.67$, $p < 0.0001$).

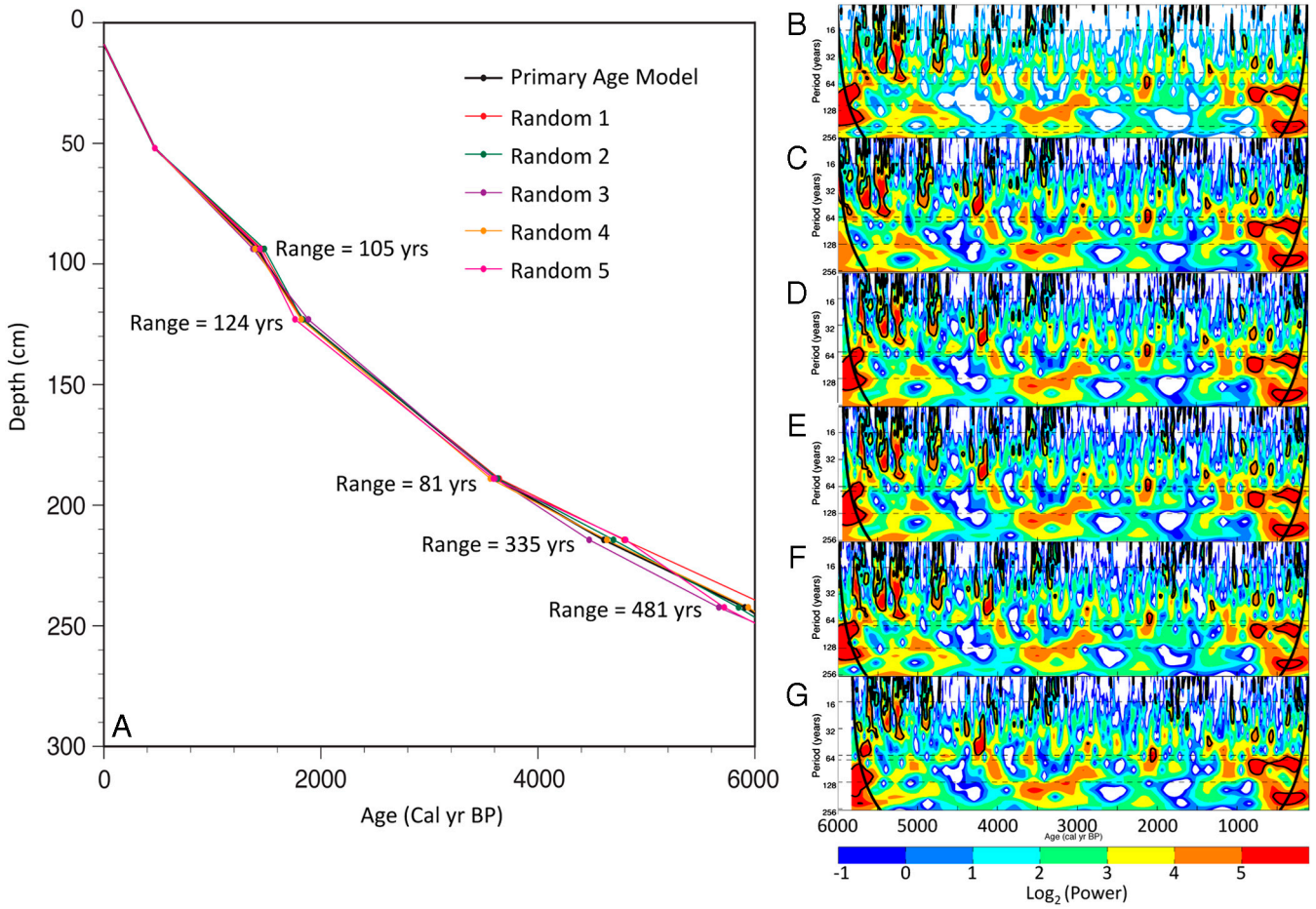

Fig. S4. Comparison of wavelet analyses using randomized age-models. Only the wavelet results are shown for brevity (i.e., global wavelet and scale-averaged data are not shown). (*A*) Original age model compared to "random 1–5" age models created using randomly generated ages within the 2σ error of each radiocarbon measurement. The range of ages between the models at each data point appears next to the curves. Wavelet analyses performed on each age model shown in panel A: (*B*) Untuned ^{14}C-only chronology (note similarity of result to Fig. 4 in main text), (*C*–*G*) as in (*B*), but for each of the 5 "random" age models. Note the similarity of the results despite the different age models. White areas on the plot have wave power less than −1 (note that this color bar is slightly different from that in the main text).

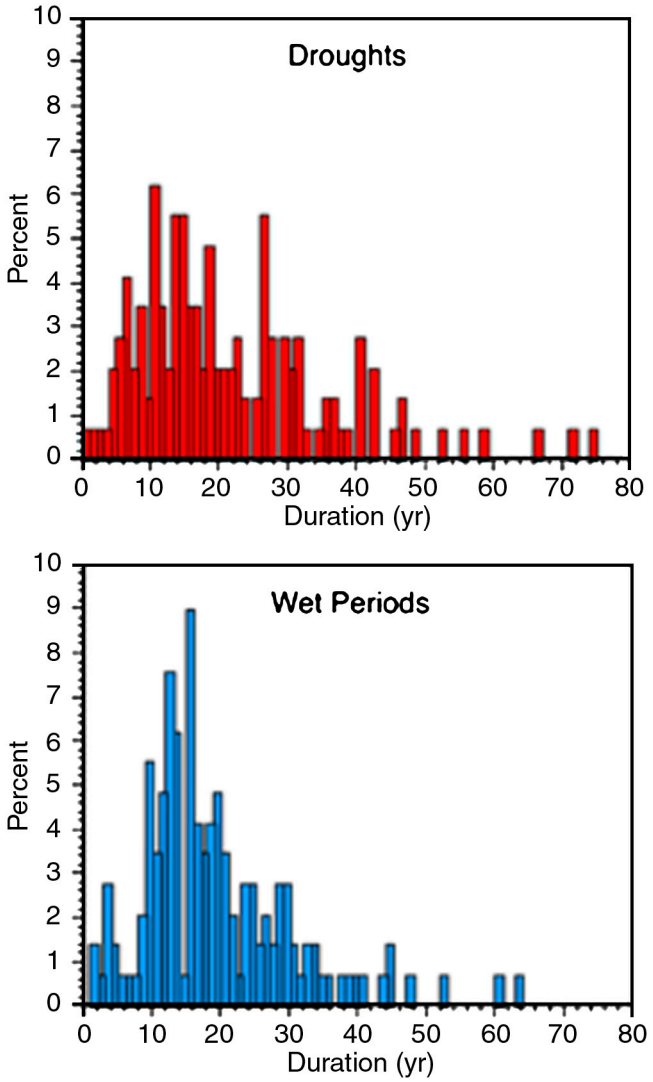

Fig. S5. Castor Lake drought/wet period frequency of occurrence as a function of duration based on the 6,000-yr-long detrended grayscale time series.

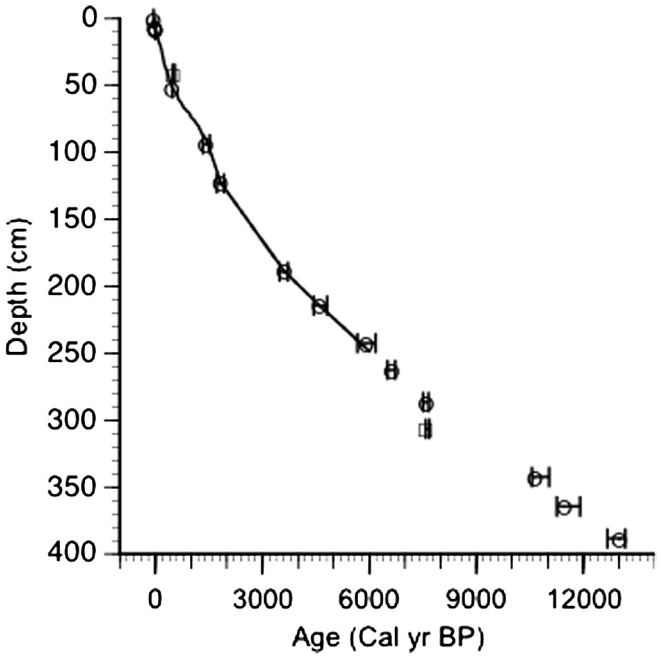

Fig. S6. Age model for Castor Lake. Sediment ages were determined by radiocarbon, tephrochronology, and ^{137}Cs analyses. Ages shown with 2σ error range. Open circles were used in the age model, whereas open squares were excluded (*SI Materials and Methods*). Line fit through the upper 6000-yr sequence shows the final PDSI-tuned age model used in this study. Note that the tuning procedure does not violate the age control data.

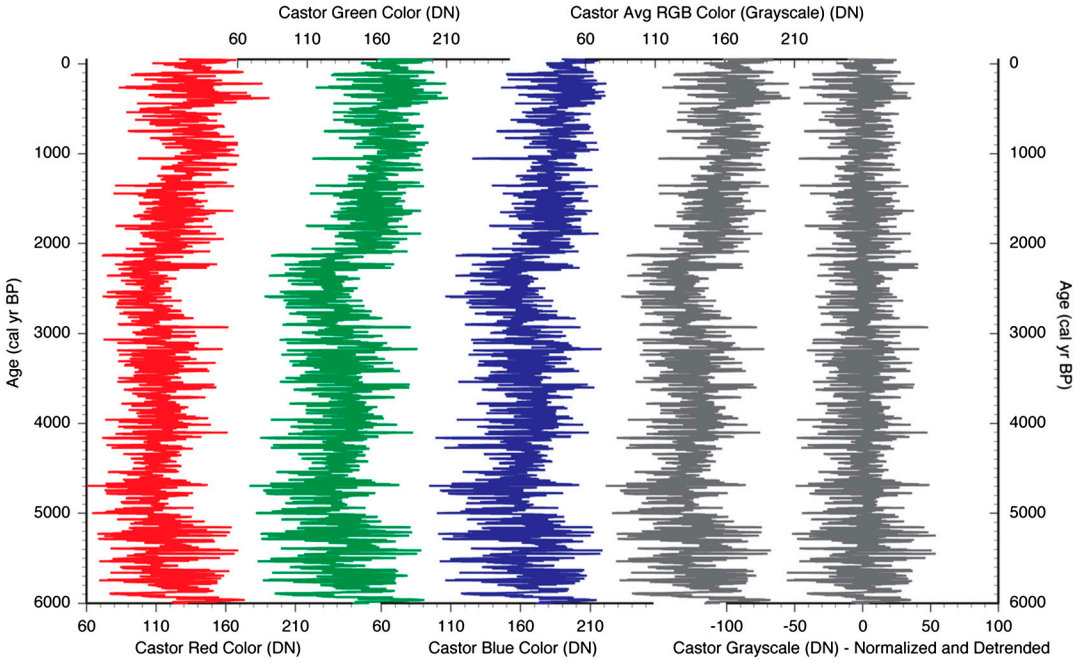

Fig. S7. Image data from Castor Lake. Raw RGB channels are color coded and labeled as such from left to right. Average RGB data (grayscale) are shown in gray before and after detrending.

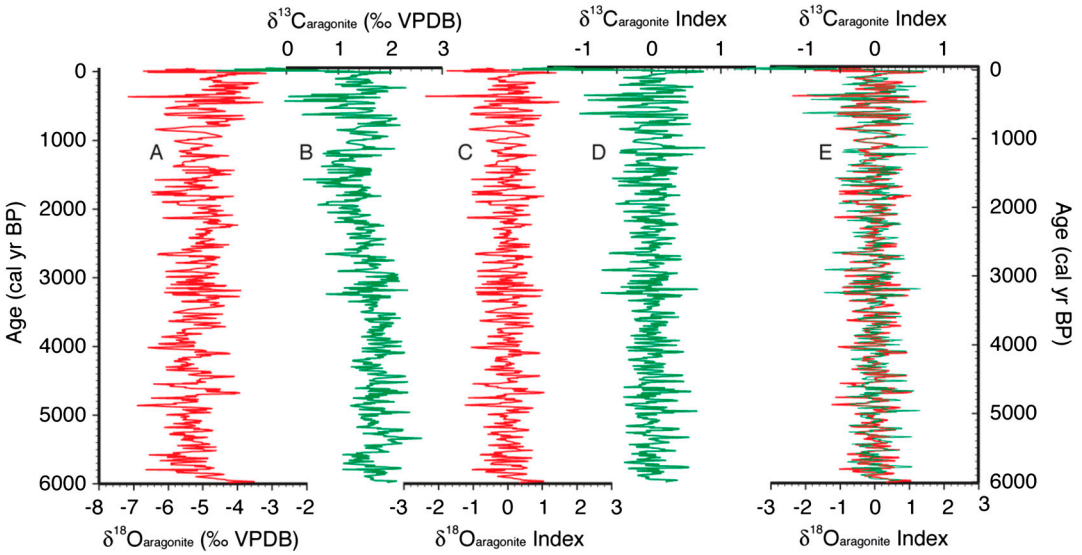

Fig. S8. Castor Lake aragonite stable isotope data (~6,000 cal yr B.P. to present). (*A*) Castor Lake $\delta^{18}O_{aragonite}$. (*B*) Castor Lake $\delta^{13}C_{aragonite}$. (*C*) Castor Lake $\delta^{18}O_{aragonite}$ after detrending and normalizing to the mean. (*D*) Castor Lake $\delta^{13}C_{aragonite}$ after detrending and normalizing to the mean. (*E*) Overlay of panels C and D ($r = 0.72$, $p < 0.00001$).

Table S1. Age control data for Castor Lake sediment record

Core	Drive depth (cm)	Total depth (cm)	^{14}C age (^{14}C yr BP) with error	Median calibrated (cal yr B.P.)	2σ calibrated age range (cal yr B.P.)	Type	Material	Lab accession number (^{14}C)
D	0	0	N/A	−55	N/A	top	N/A	N/A
D	6	6	N/A	−15	N/A	^{137}Cs	N/A	N/A
D	7.95	7.95	N/A	−10	N/A	^{137}Cs	N/A	N/A
D	8.5	8.5	N/A	−5	N/A	^{137}Cs	N/A	N/A
A	22.5	41	435 +/− 40	490	328–540	^{14}C	grass	CAMS# 104906
A	33.5	52	N/A	470	N/A	tephra	tephra	N/A
A	75.25	93.75	1530 +/− 35	1415	1334–1518	^{14}C	charcoal	CAMS# 104907
B(2)	9	123	1890 +/− 35	1835	1725–1919	^{14}C	pine needle	CAMS# 104908
B(2)	75	189	3385 +/− 35	3620	3479–3715	^{14}C	charcoal	CAMS# 104910
B(3)	8	214.4	4095 +/− 45	4610	4442–4816	^{14}C	Seed	UCI# 7527
B(3)	36	242.4	5160 +/− 100	5910	5661–6173	^{14}C	charcoal	CAMS# 104909
B(3)	56	262.4	5815 +/− 25	6630	6502–6721	^{14}C	seed	UCI# 7488
B(4)	32	286.5	6730 +/− 40	7595	7509–7654	tephra	tephra	N/A
B(4)	52	306.5	6720 +/− 80	7580	7432–7682	^{14}C	seed	CAMS# 104911
B(4)	88	342.5	9425 +/− 30	10650	10557–11035	^{14}C	seed	UCI# 7490
B(5)	16	364.5	10025 +/− 35	11465	11259–11908	^{14}C	seed	UCI# 7491
B(5)	40	388.5	11020 +/− 35	13020	12675–13169	^{14}C	seed	UCI# 7493